



ACADÉMIE
DES SCIENCES
INSTITUT DE FRANCE

Comptes Rendus

Mécanique


Vincent Longchamp, Jérémie Girardot, Damien André and Frédéric Malaise

Development of a numerical protocol for the very high strain rate dynamic fragmentation of porous-brittle materials at the microstructure scale

Volume 353 (2025), p. 1085-1108

Online since: 20 October 2025

<https://doi.org/10.5802/crmeca.328>

 This article is licensed under the
CREATIVE COMMONS ATTRIBUTION 4.0 INTERNATIONAL LICENSE.
<http://creativecommons.org/licenses/by/4.0/>



*The Comptes Rendus. Mécanique are a member of the
Mersenne Center for open scientific publishing*
www.centre-mersenne.org — e-ISSN : 1873-7234



Research article

Development of a numerical protocol for the very high strain rate dynamic fragmentation of porous-brittle materials at the microstructure scale

Vincent Longchamp^{①,*,a,b,c,d}, Jérémie Girardot^{①,b,c}, Damien André^{①,d} and Frédéric Malaise^a

^a CEA, DAM, CESTA, 33114 Le Barp, France

^b Arts et Metiers Institute of Technology, CNRS, Bordeaux INP, I2M, UMR 5295, 33400 Talence, France

^c Univ. Bordeaux, CNRS, Bordeaux INP, I2M, UMR 5295, 33400 Talence, France

^d Université de Limoges, CNRS, IRCER, UMR 7315, 87000 Limoges, France

E-mails: vincent.longchamp@protonmail.com, jeremie.girardot@ensam.eu, damien.andre@unilim.fr, frederic.malaise@cea.fr

Abstract. The discrete element method is used to study the influence of strain rate on the fracture behavior of porous brittle materials. Dynamic uniaxial tensile tests are simulated on 2D idealized samples. In such high strain rate simulation, initial and boundary conditions must be chosen carefully to achieve a uniform loading of the sample and initial conditions in order to interpret properly the results obtained. A new initial condition is developed by using an initial velocity field in accordance with the heterogeneous microstructure. High strain rates ($> 10^6 \text{ s}^{-1}$) condition have been achieved while ensuring force equilibrium. The numerical results show an increase of the maximum stress at failure, as well as the transition from single to multiple fragmentation, which are inline with experimental observations. Cracks path and stress field are also analyzed to understand the transition from single to multiple fragmentation, and an obscuration phenomenon linked to the microstructure is successfully identified.

Keywords. Discrete Element Method, fragmentation, dynamics, microstructure.

Funding. This work was supported by the French Alternative Energies and Atomic Energy Commission (CEA) and Région Nouvelle-Aquitaine.

Manuscript received 21 May 2025, revised and accepted 30 September 2025.

1. Introduction

High-strength brittle materials such as ceramics are commonly used in armoring applications where they are subjected to intense mechanical stresses. The high strain rates ($> 10^4 \text{ s}^{-1}$) encountered have a significant influence on the mechanical behavior of this kind of brittle material. The maximal stress at failure tends to increase as the strain rate increases [1], and a transition from single fracture to multiple fragmentation is observed [2]. It is widely accepted

*Corresponding author

that the microstructure plays a dominant role in the behavior and its evolution with strain rate, although the exact mechanisms involved remain to be elucidated [3].

The design of protection systems relies mainly on numerical simulation. Given the differences in size between microstructures ($\sim \mu\text{m}$) and macrostructures ($> \text{mm}$), materials are generally modelled at macroscopic scale as equivalent-homogeneous materials. In such simulation, where inhomogeneities and local phenomenon are not represented, the effects of strain rate must be explicitly taken into account in the behavior and damage laws of the materials [2,4]. These laws, whether based on micromechanical or phenomenological considerations, need to be calibrated with experimental values on the material of interest, which is a rather difficult task. This can be a tedious stage, particularly if the goal is to study several materials and optimise the microstructure to obtain the best performance. In addition, the strain rate range that can be experimentally explored is limited, in particular by the size of the sample [5,6]. Finally, the detailed study of the phenomena governing the behavior of materials under extreme stress is very complex, given the very short characteristic times and small scales involved.

Various methods for linking microstructure and behavior without recourse to experiment have therefore emerged, namely analytical approaches [7] and numerical approaches with micromechanical simulation [8]. Analytical laws take as input a population of defects, often idealised in the form of pore and/or crack distributions [5,7,9]. Several simplifying assumptions make their application limited and unsuitable for material with complex porosity (like plasma sprayed ceramics with a lot of pores of various shape and interconnected cracks) [10]. Micromechanical simulation consists of directly including the microstructure geometrically in a numerical model in order to deduce the equivalent homogeneous behavior by applying elementary loading conditions [11]. Several studies have been carried out to identify the evolution of maximal stress as a function of strain rate on real microstructures [12–14]. Micromechanical models are usually not suitable for direct simulation of experimental tests. As they require a very refined mesh in order to model accurately the microstructure, computing resources can quickly become excessive when dealing with macroscopic structure. Therefore, they are often coupled with multi-scale modeling, where standard loadings are applied on elementary volume at the microscopic scale to assess their behavior and implement it in a macroscopic homogeneous model [15]. For instance, a Dynamic Increase Factor (DIF) representing the increase in strength with strain rate is commonly adopted to capture the effect of the microstructure on stress at high strain rate in a homogenized model. Damage models in the Finite Element Method framework (for example in [16]), or more recently in the DEM framework [17], can also be considered to use the results of microscale simulations.

The aim of this work is to set up a simulation framework for studying the role of the microstructure of brittle materials on their dynamic behavior. To this end, a micromechanical approach based on the Discrete Element Method (DEM) is developed. This numerical method is considered for its ability to model complex heterogeneous brittle media and cracking [18–21]. Additional efforts have recently been made to build 3D simulations using the DEM [22]. These simulations further supported the relevance of the method, although those involved in the microscale dynamic analysis are currently limited to aggregate-based materials such as concrete [23,24] under compressive loadings and strain rates below 100 s^{-1} . This relatively low strain rate and the large sample sizes, due to the significant heterogeneity scale in concrete, allow for direct and qualitative comparisons with experimental observations.

The proposed study addresses much higher strain rates and smaller porosity sizes and proposes here a protocol to analyze microstructures under extreme loading conditions, enabling the study of material behavior at very high strain rates.

Section 2 sets out the conditions required to establish a uniform load in the dynamic regime. Then, the DEM framework and the generation of the numerical sample are presented in Sec-

tions 3 and 4 respectively. In Section 5, three protocols are proposed and applied to an idealised porous ceramic. The numerical results are presented and analysed in Section 6. All simulations are performed on 2D idealized microstructures comprising only circular pores. This choice was made to facilitate the analysis of results and the comparison of protocols, given that the objective of this work is to propose a high-speed deformation simulation protocol free from equilibrium issues. Of course, obtaining results representative of a real material would require precisely characterizing the microstructure of said material and performing 3D simulations, as the 2D assumption can rarely be applied in real cases. Subsequently, the effect of density, elastic modulus and sample length on the strain rate effect are explored in Section 7. Finally, as a demonstration of its capabilities, the developed protocol is applied to a real microstructure in 3D in Section 8, whose data comes from a previous study [20], where a complex 3D heterogeneous porosity pattern associated with a network of nano-cracks makes very challenging any fragmentation simulations and analysis at the microstructure scale.

2. Forces equilibrium condition

In the case of a uniaxial stress loading, the forces applied on both ends of a sample must be equal (force equilibrium) in order to achieve a homogeneous stress state. This balance depends on the time required for the stress wave to travel through the sample, which is a function of both the length L of the sample along the loading direction and the acoustic wave celerity (C_0) defined by equation (1):

$$C_0 = \sqrt{E/\rho}, \quad (1)$$

where E is the elastic modulus and ρ is the density. So, an equilibrium time (t_{eq}) can be defined with equation (2):

$$t_{\text{eq}} = n \times L/C_0, \quad (2)$$

where n is the number of time the wave travel through the sample. This number must be greater than 3 – 4 to achieve a homogeneous state [6].

A second characteristic time is the failure time (t_{fail}) at which the sample failure begins to occur. This time can be expressed with the failure strain ϵ_f and the strain rate $\dot{\epsilon}$ (considered constant) with equation (3):

$$t_{\text{fail}} = \epsilon_f / \dot{\epsilon}. \quad (3)$$

To ensure that the sample is at equilibrium when the failure starts, inequality (4) must be verified:

$$t_{\text{fail}} > t_{\text{eq}} \implies \dot{\epsilon} < \frac{\epsilon_f \times C_0}{n \times L}. \quad (4)$$

Considering an elastic linear behavior until failure, Hook's law leads to $\sigma_f = E \times \epsilon_f$, where σ_f is the stress at failure, inequality (4) becomes:

$$\dot{\epsilon} < \frac{\sigma_f}{n \times L \sqrt{\rho E}}. \quad (5)$$

Equation (5) gives an estimation of the maximal strain rate that can be obtained by loading a relaxed sample while preserving the forces equilibrium, and thus a homogeneous stress and strain state in the sample [6]. One can note that it is possible to increase the maximal strain rate by decreasing the sample dimension L . However, the sample dimension must be large enough to be representative of the whole material.

This restriction is the main motivation for this work, as currently no experimental or numerical study can achieve very high strain rate while ensuring a homogeneous stress and strain field in the sample. Nonetheless, as Song [6] points out, several numerical studies [25,26] are above this limit and results can be quite difficult to interpret when equilibrium is not achieved [13,14].

3. Discrete Element Method

The Discrete Element Method (DEM) is used to perform the numerical simulation of crack propagation under dynamic mechanical loading of brittle porous materials. These kinds of methods are commonly used to simulate the behavior of heterogeneous brittle materials like ceramics, rocks and concrete, under static [27] or dynamic loading [21]. Indeed, its discrete nature makes it a useful alternative to continuous methods such as Finite Element Method (FEM) to model complex heterogeneous microstructure of materials containing pores and cracks [19,28]. It can also handle naturally discontinuous phenomenon like multi-fragmentation and the interaction of fragments with different contact laws [17,18].

With this method, a continuous medium is represented by a set of rigid discrete elements (DE) that interact through a lattice bond network. DE are typically spherical and treated as rigid bodies, while the bonds impart mechanical behavior to the assembly. The GranOO [29] platform is used in this work, and the behavior of the bonds is modeled with cylindrical Euler–Bernoulli beams. The detailed expression of forces and momentum according to displacement and rotation can be found in [30].

3.1. Cracking criterion

Crack propagation is modeled by deleting bonds (which are cylindrical Euler–Bernoulli beams) whose stress is higher than the selected threshold $\sigma_{\text{threshold}}$. The stress inside a beam is assessed with the equivalent Rankine stress σ_{eq} defined with equation (6):

$$\sigma_{\text{eq}} = \frac{1}{2} \left(\sigma_{N_{\text{max}}} + \sqrt{\sigma_{N_{\text{max}}}^2 + 4\tau_{\text{max}}^2} \right), \quad (6)$$

where $\sigma_{N_{\text{max}}}$ is the maximal normal stress (from bending and tensile) and τ_{max} is the maximal contribution of torque, whose detailed expression can be found in [31].

3.2. Numerical time scheme

At each time step, the acceleration a of each DE is computed thanks to the dynamical equilibrium principle by knowing all the forces F applied on the DEs. Then, new velocities v and positions p are computed with an explicit scheme: the velocity Verlet [30] (equation (7)), which involve no damping:

$$\begin{aligned} a_{n+1} &= \sum F_{n+1} / m_{\text{DE}}, \\ v_{n+1} &= v_n + \Delta t (a_n + a_{n+1}) \times 0.5, \\ p_{n+1} &= p_n + v_{n+1} \Delta t + 0.5 \times a_{n+1} \Delta t^2, \end{aligned} \quad (7)$$

where m_{DE} is the mass of the DE and the subscripts n or $n+1$ indicate the iteration. In all simulations, the time step Δt is selected to be equal to 15% of the most critical time step Δt_c according to the CFL condition defined by equation (8):

$$\Delta t_c = \sqrt{\frac{\min(m_{\text{DE}})}{\max(K_{\text{Beam}})}}, \quad (8)$$

where K_{Beam} is the stiffness of a beam (in tensile, bending or torque mode as described in [20]).

4. Generation of numerical sample

4.1. Isotropic homogeneous sample

A 2D model (Figure 1) of a square sample of size $L_0 = 1 \mu\text{m}$ without porosity is firstly created with the generation procedure included in the GranOO platform [29]. DE are generated at random positions with a radius following a uniform distribution ($\pm 12.5\%$) around the selected mean value. The generation algorithms stop when the average contact number per DE is 4.5, which is the optimum value for generating 2D domains (determined by trial and error). The DE are then connected to their nearest neighbors through an iterative algorithm that artificially grows the DE, aiming to reach an average of 6.1 bonds per DE. This procedure yields a set of compact DE representing an isotropic homogeneous continuous medium. In the present model, the mean DE radius R_{DE} is set on $0.0033 \mu\text{m}$, leading to a total of 26383 DE, which is enough to have a converged macroscopic behavior [30].

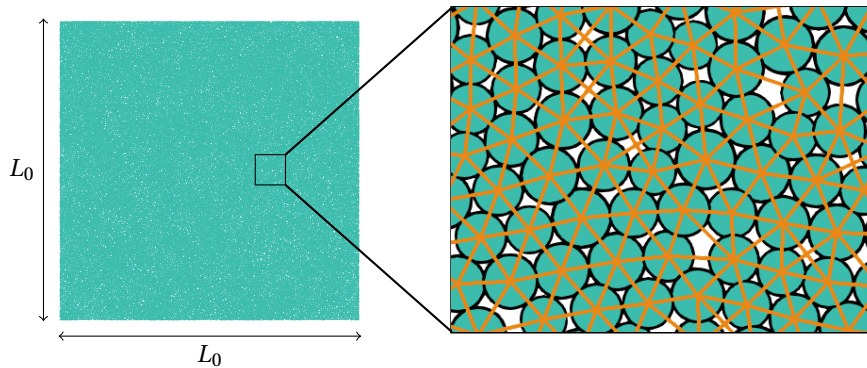


Figure 1. Dense sample represented with DEM as a set of DE (blue) linked by cohesive beam (orange).

The mechanical behavior of this homogeneous sample is selected to correspond to a dense ceramic-like material, whose mechanical properties are summarized in Table 1, with E the elastic modulus, ν the Poisson coefficient, ρ the density and σ_f the stress at failure under tensile loading.

Table 1. Mechanical properties of dense material.

E [GPa]	ν [-]	ρ [kg/m^3]	σ_f [MPa]
220	0.30	6060	200

Nevertheless, these macroscopic parameters cannot be directly used as an input of the discrete model (parameters of beams and DE). Indeed, the mechanical behavior of the discrete medium at the macro-scale is controlled by the behavior of the beams between DE, and there is no direct relationship between the macroscopic behavior and the properties of the beams. Hence, determining the mechanical parameters of the beams requires a calibration procedure to match the macroscopic behavior of the material. Here, the beams are calibrated with tensile tests according to the procedure described in [30]. The obtained parameters are summarized in Table 2, where E_B is the elastic modulus, ν_B is the Poisson coefficient, σ_B^f is the failure threshold related to σ_{eq} (equation (6)) and R_B is the beam radius. The subscript B is used to indicate that these are beams parameters. These parameters are uniform throughout all the beams,

only the beam lengths vary, as they depend on the distance between the two linked DE. Some authors [15,32] propose to introduce variability in the beams strength, this is employed to artificially take into account small defects present in real material [32] and is usually used in multi-scale modelling [15]. This is out of the scope of this study, which focuses on a perfectly homogeneous material in which defects will only be created explicitly by introducing porosities into the mesh.

Table 2. Mechanical and geometrical properties of the beams.

E_B [GPa]	ν_B [-]	σ_B^f [GPa]	$R_B/\overline{R_{DE}}$ [-]
2865	0.30	4	0.30

To compensate the void between the spherical discrete elements, the density of the DE (ρ_{DE}) is set according to the whole volume of all DE (V_{DE}^{tot}) with equation (9):

$$\rho_{DE} = \rho \times V / V_{DE}^{tot}, \quad (9)$$

and the sample macroscopic volume V is computed with equation (10), by considering a thickness of the 2D sample equal to the average DE diameter:

$$V = 2 \times \overline{R_{DE}} \times L_0^2. \quad (10)$$

4.2. Porous sample

A porous sample (Figure 2) is generated from the previous dense one (Figure 1) by including spherical pores of radius R_p at random location and deleting DE, until the void fraction f (equation (11)) reaches at least 10%:

$$f = 1 - (\rho_p / \rho), \quad (11)$$

where ρ_p is the macroscopic density of the porous sample, computed with equation (9).

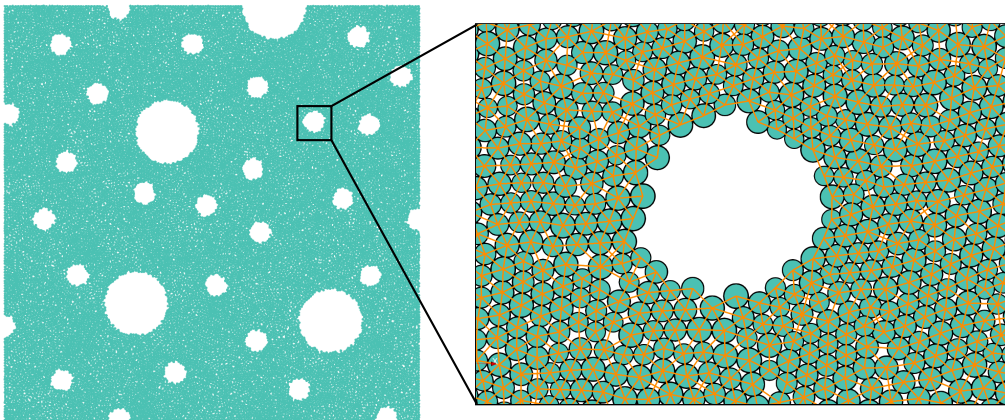


Figure 2. Porous numerical sample.

All the geometrical parameters are summarized in Table 3. The minimal pore size is selected to be at least five times higher than the DE size to achieve a sufficiently accurate modeling.

Mechanical properties of the porous sample are computed with a virtual tensile test, the values are reported in Table 4, the parameters of the dense material are also indicated for comparison. The wave celerity C_0 is calculated with equation (1).

Table 3. Geometrical parameters of the porous sample.

L_0 [μm]	$\overline{R_{DE}}$ [μm]	R_p [μm]	N_{DE}	f [%]
1	0.0033	0.025 and 0.075	23348	11.53

Table 4. Mechanical properties of the dense and porous materials.

Material	E [GPa]	ν [-]	ρ [kg/m^3]	σ_f [MPa]	C_0 [m/s]
Dense	220	0.30	6060	200	6025
Porous	150	0.32	5365	68	5288

In this study, it is important to emphasize that no strain rate sensitivity is included in the behavior of the beam network. In addition, the absence of significant numerical damping was also checked with elastic wave propagation simulations.

5. Numerical simulation protocol

This section details the simulation protocol set up, and the boundary condition used to apply the loading and the different initial conditions considered.

5.1. Mechanical loading and boundary conditions

The sample is submitted to a uniaxial stress loading in the \vec{x} direction as described on Figure 3. This is achieved by blocking the normal displacement ($U_x = 0$) of all the DE on the left hand side (X_{\min}), while a normal speed V_x is applied on the DE of the opposite sides (X_{\max}). Top and bottom sides remain free.

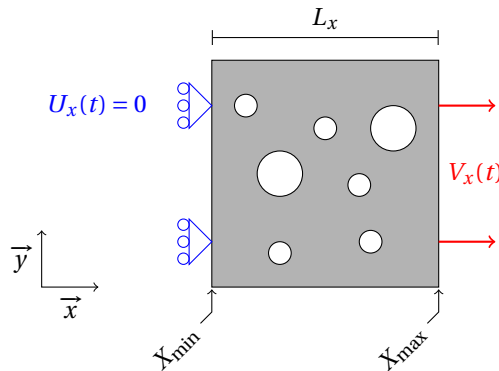


Figure 3. Boundary conditions of the numerical 2D tensile test.

5.2. Stress and strain monitoring

Apparent global strain ϵ_{xx} and apparent global strain rate $\dot{\epsilon}_{xx}$ in the loading direction are computed with equation (12):

$$\epsilon_{xx}(t) = \frac{L_x(t) - L_0}{L_0} \quad \text{and} \quad \dot{\epsilon}_{xx}(t) = \frac{d\epsilon_{xx}}{dt} = \frac{V_x(t)}{L_0}, \quad (12)$$

where L_0 is the initial length and $L_x = X_{\max} - X_{\min}$ is the current length of the sample along \vec{x} .

Total resulting normal forces $F_{X_{\min}}$ and $F_{X_{\max}}$ on sides X_{\min} and X_{\max} are measured (sum of all the forces \vec{x} components applied on the DE at the X_{\min} and X_{\max} boundaries), and used to compute the stress on each side (equation (13)):

$$\sigma_{X_{\min}} = F_{X_{\min}} / S_0 \quad \text{and} \quad \sigma_{X_{\max}} = F_{X_{\max}} / S_0, \quad (13)$$

where S_0 is the initial section computed with equation (14) by considering that the thickness of the sample (\vec{z} direction) is equal to the average DE diameter (the same convention has been used in equation (10) to compute the macroscopic volume):

$$S_0 = 2 \times \overline{R_{\text{DE}}} \times L_0. \quad (14)$$

Finally, the average stress $\bar{\sigma}$ in the sample is estimated with equation (15):

$$\bar{\sigma}_x = 0.5 \times (\sigma_{X_{\min}} + \sigma_{X_{\max}}). \quad (15)$$

5.3. Initial velocity field

Three different cases of initial velocity fields are tested and so-called: *static*, *linear* and *heterogeneous*.

5.3.1. Static (\mathcal{V}_0)

Static condition (equation (16)) is close to an experimental test, the velocity of each DE i is null at the beginning of the simulation:

$$\vec{V}_i(t=0) = \vec{0}. \quad (16)$$

The velocity $\vec{V} = V_x \vec{x}$ of DE on the side X_{\max} is increased from 0 to V_{\max} smoothly in a time Δt beyond which it remains constant according to equation (17). The time evolution of velocity is represented on Figure 4.

$$V_x(t) = \begin{cases} V_{\max} \times \frac{1}{2} \left[1 + \sin\left(\frac{2\pi t}{\Delta t} - \frac{\pi}{2}\right) \right] & \text{if } 0 \leq t \leq \Delta t, \\ V_{\max} & \text{if } \Delta t \leq t. \end{cases} \quad (17)$$

To achieve an equilibrium state (i.e. $F_{X_{\min}} = F_{X_{\max}}$), the loading must be applied slowly enough (in relation to the characteristic equilibrium time t_{eq} , cf. Section 2). So the rising time Δt is set to be above the equilibrium time t_{eq} .

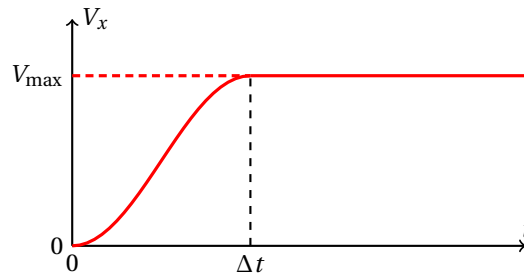


Figure 4. Loading velocity.

According to the geometrical and mechanical parameters of the porous sample (Tables 3 and 4), equation (2) gives $t_{\text{eq}} = 0.75 \text{ ns}$ (with $n = 4$) and equation (5) leads to $\dot{\epsilon}_{\max} = 6 \times 10^5 \text{ s}^{-1}$. Higher strain rate values cannot be achieved as the failure would occur before the strain rate

reaches its constant maximal value. And Δt cannot be decreased below t_{eq} to reach the target strain rate faster, as it would induce a non equilibrium of the forces inside the sample [33].

5.3.2. Linear (\mathcal{V}_L)

In DEM numerical simulation, with its explicit time scheme, it is possible to use non static initial conditions, with for example a linear velocity field in the sample [12,34], where the initial velocity of each DE i depends on its position X_i along the loading direction \vec{x} , as described by equation (18):

$$\vec{V}_i(t=0) = \frac{X_i - X_{min}}{X_{max} - X_{min}} \times V_{max} \times \vec{x}. \quad (18)$$

This allows to have a uniform strain rate (equation (12)) in the whole sample, which does not evolve with time (red dashed line on Figure 4). This velocity gradient is only applied along \vec{x} (Figure 5), the component along the \vec{y} axis is null in the initial state. This linear evolution assumes that the strain is homogeneous in the whole sample, which is not true for heterogeneous material submitted to uniform loading. Moreover, the Poisson effect (strain along \vec{y}) is also neglected.

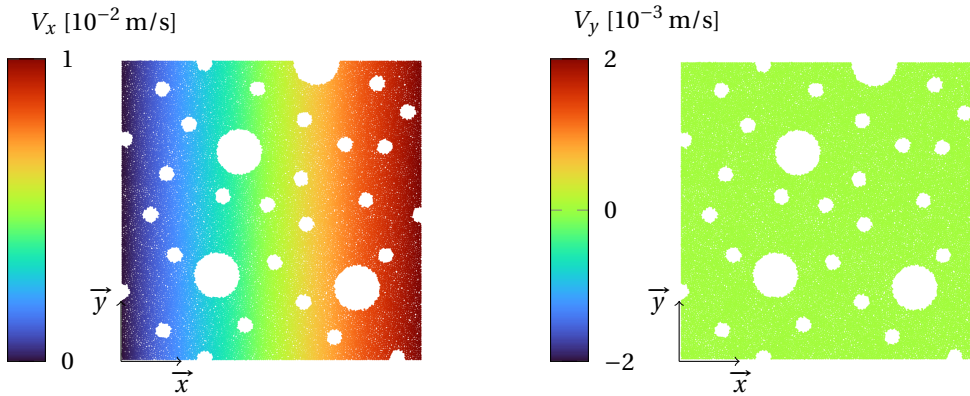


Figure 5. Velocity field at initial state for the \mathcal{V}_L condition (linear along \vec{x} and null along \vec{y}).

5.3.3. Heterogeneous (\mathcal{V}_H)

The heterogeneous condition has been developed in order to take into account heterogeneity and Poisson effect, allowing to overcome the shortcomings of the currently available simulation protocols for carrying out very high strain rate simulations on heterogeneous medium.

A preliminary computation is performed at low strain rates, from an initial static velocity field. Then the velocity field in the sample is recorded when the behavior is still in a quasi-stationary state in the elastic domain (very low deformation). This velocity field \vec{V}_i^0 is normalized and multiplied by the target velocity V_{max} (equation (19)) to be used as the starting point of a second simulation:

$$\vec{V}_i(t=0) = \vec{V}_i^0 \times \frac{V_{max}}{V_{max}^0}, \quad (19)$$

where exponent 0 refers to values obtained during the preliminary computation. This preliminary computation is performed with $V_{max}^0 = 0.01$ m/s and the recorded velocity fields at $\epsilon_{xx} = 10^{-6}$ along \vec{x} and \vec{y} are plotted on Figure 6.

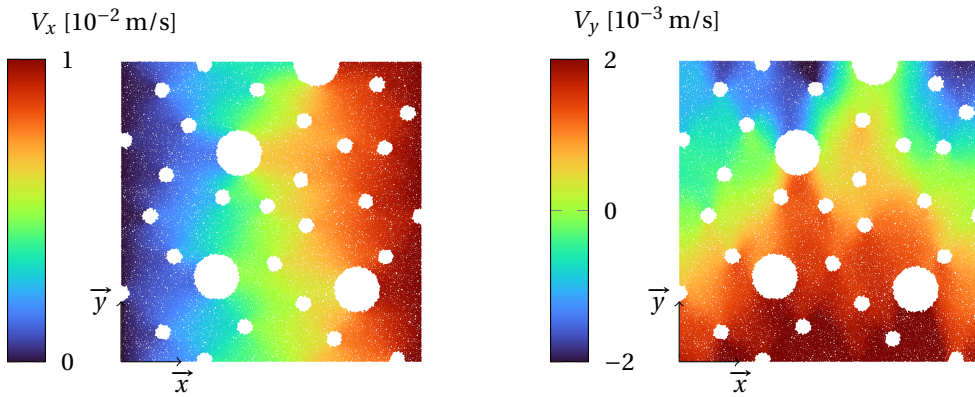


Figure 6. Velocity field at initial state used for the \mathcal{V}_H condition (heterogeneous).

6. Results and analysis

6.1. Stress-strain curve

For each initial configuration (\mathcal{V}_0 , \mathcal{V}_L , \mathcal{V}_H), dynamic tensile loading simulations are performed with various strain rates as described in Section 5. Stress-strain curves are plotted on Figure 7, stress on each sample side (X_{\min} and X_{\max}) are plotted in dotted and dashed lines, and the average stress $\bar{\sigma}_x$ is the solid line. The minimal strain rate applied is 10^4 s^{-1} . The lower the strain rate, the longer the computation time, because low strain rate leads to longer time to reach the failure (equation (3)). As the time steps is fixed by the explicit resolution, more iterations, and thus computation time, are required to reach the failure at low strain rate. Nonetheless, this strain rate is used as the reference “quasi-static” response of the sample as no strain rate effect can be observed at this level (no difference between the curves at 10^4 s^{-1} and 10^5 s^{-1}). For the lowest strain rates (10^4 s^{-1} to 10^6 s^{-1}), the behavior is the same regardless of the protocol used. Differences arise for strain rate above 10^6 s^{-1} .

As expected, for the protocol \mathcal{V}_0 (Figure 7(a)), there is no equilibrium when the strain rate is higher than 10^6 s^{-1} and the sample start to break before reaching the target strain rate of 10^7 s^{-1} and 10^8 s^{-1} . Hence, the strain rate value for these simulations is recorded when the maximal stress is achieved. The stresses on each side are not the same during the loading phase, and even the average stress does not increase linearly during the initial elastic loading before failure (red curve corresponding to $\dot{\epsilon}_{\max} = 4 \times 10^6 \text{ s}^{-1}$ on Figure 7(a)).

When using the linear protocol \mathcal{V}_L (Figure 7(b)), the slope of the stress-strain curves increase with the strain rate. This behavior is not valid and is due to the simplification of the initial velocity field. The linear form of the velocity field assumes that the material is homogeneous. Thus, the elastic modulus at the first instants of the simulation corresponds to the modulus of the dense material without pores (220 GPa, see Table 4): for $\dot{\epsilon}_{xx} = 10^8 \text{ s}^{-1}$, the average modulus between $\epsilon_{xx} = 0$ and $\epsilon_{xx} = 2 \times 10^{-4}$ is 226 GPa. In low strain rate simulations (10^4 – 10^6 s^{-1}), the velocity field reach equilibrium quickly enough to observe linear behavior with a slope corresponding to the modulus of the porous material. However, when the strain rate is higher (10^7 – 10^8 s^{-1}), there is not enough time to achieve equilibrium, resulting in a modulus that seems to increase with increasing strain rate. This is an example of an inertia artifact that can be misleading when analyzing results.

The simulations performed with protocol \mathcal{V}_H (Figure 7(c)) do not exhibit any increase of the slope with strain rate and the equilibrium is achieved. A clear increase of the maximal stress on

the stress-strains curves is observed with increasing strain rate.

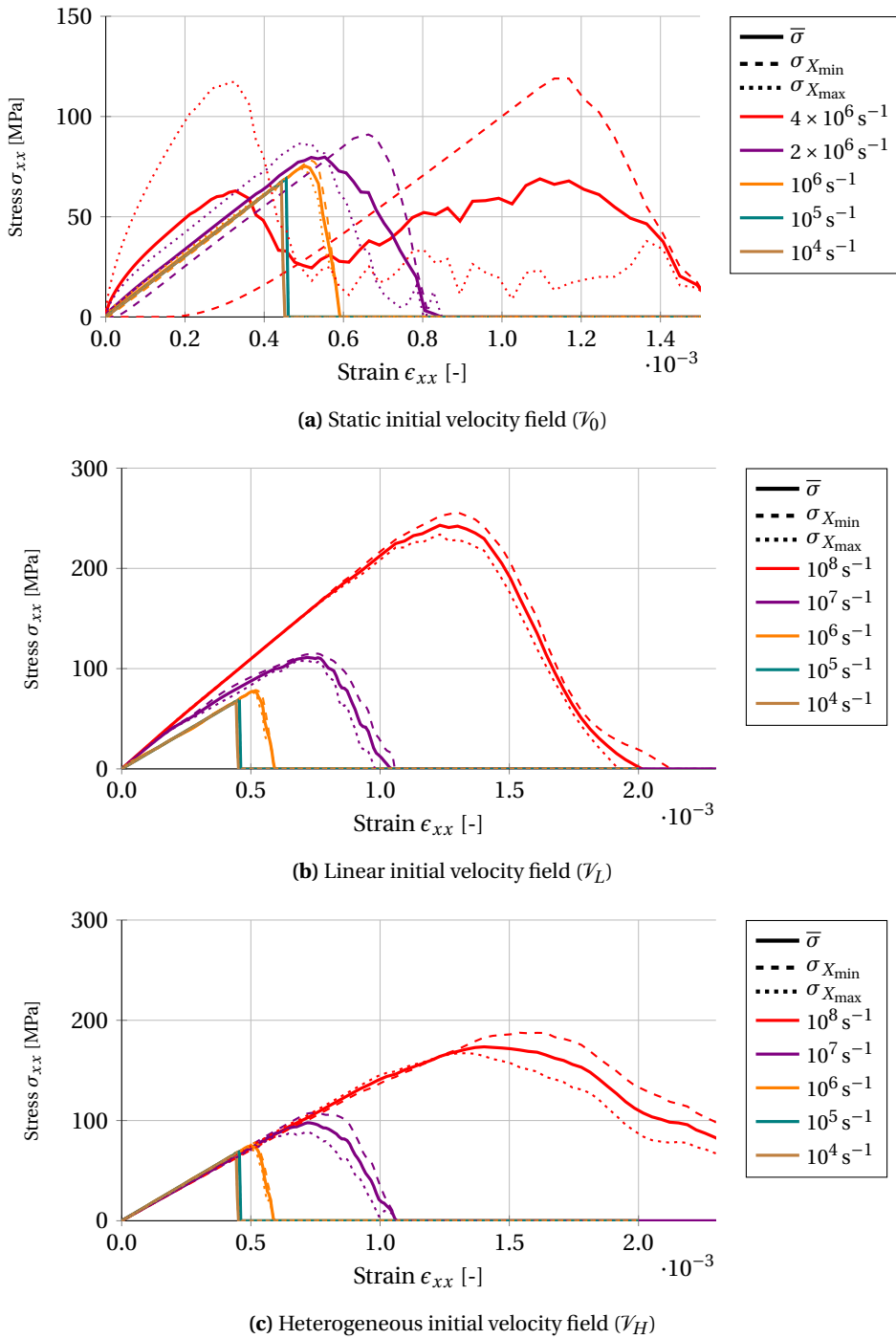


Figure 7. Evolution of stress-strain for strain rates ranging from 10^4 s^{-1} to 10^8 s^{-1} for the three initial velocity conditions.

The ultimate tensile stress (UTS) of each simulation is reported on Figure 8. Values obtained with protocol \mathcal{V}_L are higher than the ones obtained with protocol \mathcal{V}_H due to the increase of modulus with increasing strain rate. The values obtained with protocol \mathcal{V}_H follows the power law introduced by Kimberley [1] which is commonly used to describe the UTS evolution with strain rate. In this case $\sigma_0 = 68 \text{ MPa}$ and $\dot{\epsilon}_0 = 5.3 \times 10^7 \text{ s}^{-1}$ is determined by fitting the curve.

Based on the previous results, it is clear that the \mathcal{V}_0 protocol does not allow for high strain rate simulation and the \mathcal{V}_L protocol is not suitable for heterogeneous materials, as it induces a non-physical increase in the elastic modulus, which alters the maximum stress values obtained. This problem is solved with the \mathcal{V}_H protocol, which will be used exclusively from now on.

6.2. Evolution of crack density

For the \mathcal{V}_H protocol, the number of broken beam is plotted on Figure 9(a) in order to follow the crack generation and propagation. The incipient failure (increase of broken beam) occurs at the same strain — and thus stress — for each strain rate. This is expected as the behavior of the beam is not sensitive to the strain rate. However, the crack creation and propagation (evolution of broken beam with time) is affected by the strain rate level. For strain rate 10^4 s^{-1} , there is a sharp increase at failure and then the broken beam number stays constant. For higher strain rate ($>10^6 \text{ s}^{-1}$), the broken beams number increases more progressively with the strain. However, this should not be interpreted as slower crack propagation: in a fixed amount of time the crack propagates of the same distance regardless of the strain rate, but at higher strain rate, the strain increases more for the same amount of time, resulting in a lower slope of cracking versus strain curve. Besides, at high strain rate, the broken beam number keeps increasing after the peak stress has been reached and even when the average stress is null, this is due to inertia effect. Broken beam number at max stress and when stress is null for each strain rate are reported on Figure 9(b). For low strain rate, both values are close and when the strain rate increase, broken beam number increase, the gap between the value at maximal stress and null stress also increase significantly. This is coherent with experimental results where fragmentation density tends to increase with increasing strain rate [7].

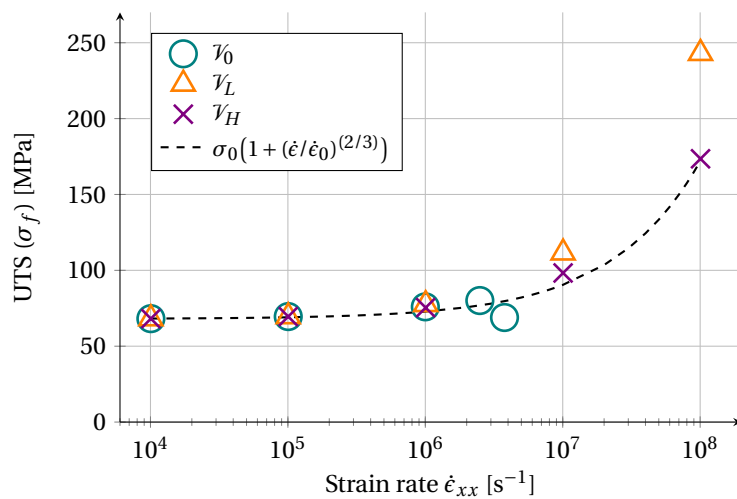


Figure 8. Ultimate tensile stress as a function of strain rate for each simulation protocol.

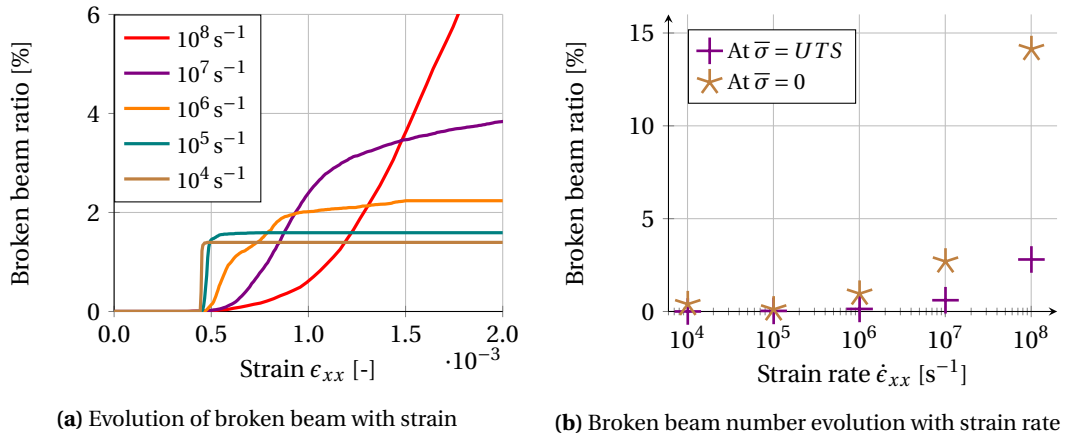


Figure 9. Broken beam ratio for \mathcal{V}_H protocol.

6.3. Stress field and cracking pattern

In this section, only the heterogeneous protocol \mathcal{V}_H is used as it gives better results, inline with experimental observations. The evolution of the stress field σ_{xx} (Virial [31]) in the sample is represented on Figure 10 for a “low” strain rate ($\dot{\epsilon}_{xx} = 10^5 \text{ s}^{-1}$) and a “high” strain rate ($\dot{\epsilon}_{xx} = 10^7 \text{ s}^{-1}$). The crack generation and propagation are visualised by representing only the beams in black: cracks appear in white when beams are deleted.

In both simulations the initial stress field is the same, with stress concentration around the pores. The maximal stresses zone are located near the biggest pores and thus the first crack starts from the same location in both simulation (the largest pore on the upper edge).

In the “low” strain rate simulation (Figure 10(a)), few cracks propagate from the top to the bottom of the sample. This propagation is associated with a relaxation of stresses (blue area) around the cracks, hence all the pores in these relaxed zone can no longer initiate new cracks, they are “obscured” according to the theory developed by [3]. Finally, only few cracks have been created from the largest pore until the sample is fully fractured in two main pieces.

At “high” strain rate (Figure 10(b)), the first crack initiates from the same location (the big pore on the upper edge). However, the strain rate being faster, the stress level around other pores increases a lot before they are “obscured”. Hence, small pores that did not lead to crack initiation in the “low” strain rate simulation can create stress concentration that initiate new cracks. Before total failure of the sample ($t = 0.09 \text{ ns}$) almost every pore has initiated a crack and at the end ($t = 0.20 \text{ ns}$), the sample is fractured in multiple pieces.

This switch of cracking pattern, with an increasing number of cracks and generated fragment is in agreement with reported experimental observation [2,3].

6.4. Influence of sampling for the same distribution

The \mathcal{V}_H protocol has been identified as the most promising to perform simulations at high strain rates. Further validation of this protocol is conducted by performing simulations on other randomly generated microstructures. The initial homogeneous sample is always the same (see Figure 1), only the pore location inside the sample changes. Pores cannot be connected, but there might be open porosities (connected to an edge). Large pores ($R = 0.075 \mu\text{m}$) are generated

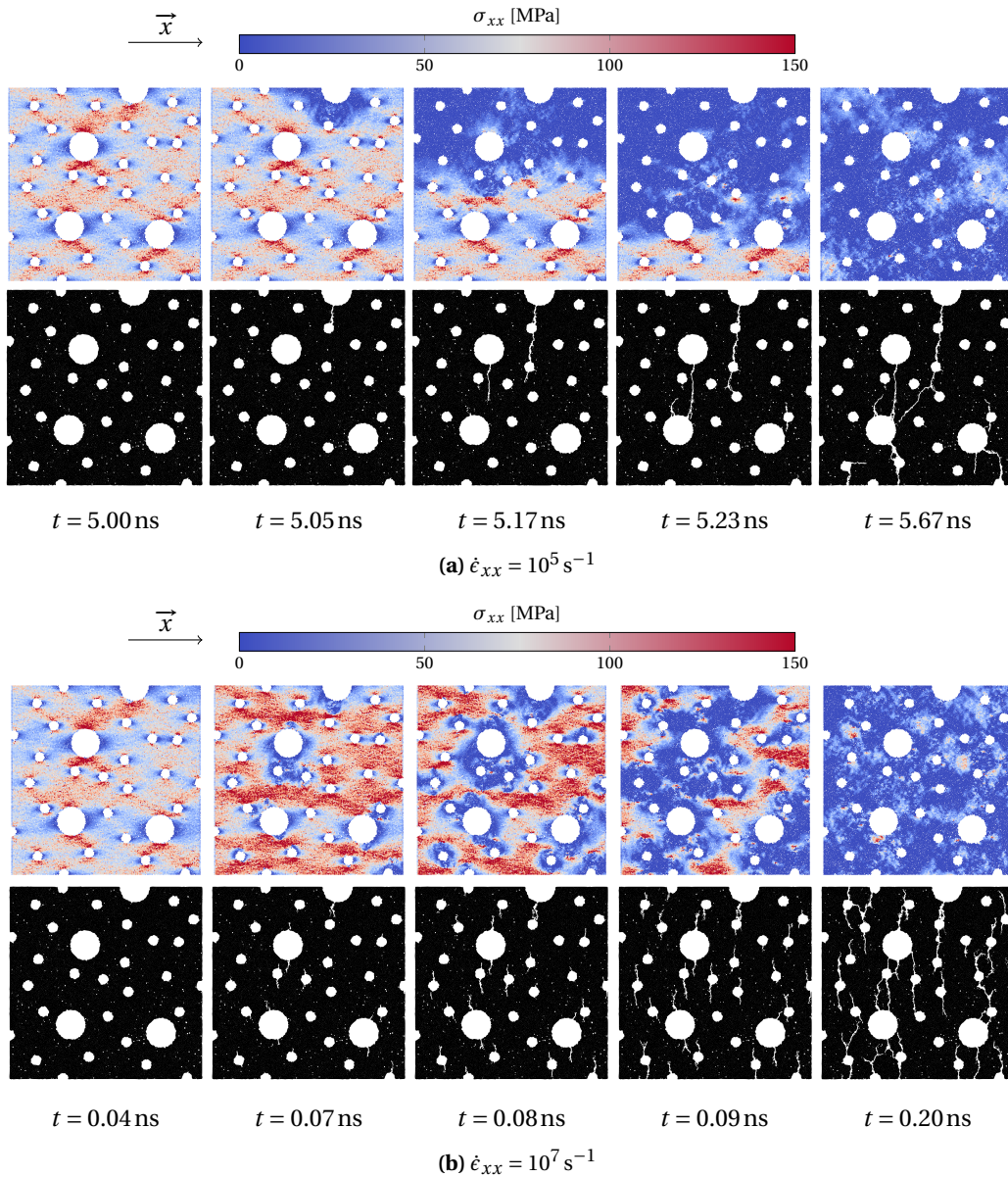


Figure 10. Evolution of the stress field (virial) σ_{xx} in the sample, and the crack propagation (beam represented in black).

in a first step until the void fraction reaches 5.5 %, then small pores ($R = 0.025 \mu\text{m}$) are generated until the void fraction reaches at least 10 %. This is performed to have the same porosity size distribution across all samples. Nine new samples are generated, three of them are represented in Figure 11. The mean void fraction (including the first sample) is 11.09 % with a standard deviation of 0.42 %.

Tensile tests are performed according to the \mathcal{V}_H protocol with a strain rate from 10^5 s^{-1} to 10^8 s^{-1} . Of note that the initial velocity field being dependent of the microstructure, it is different for each sample. Simulations at $\dot{\epsilon} = 10^4 \text{ s}^{-1}$ have not been performed as previous results (Figure 7)

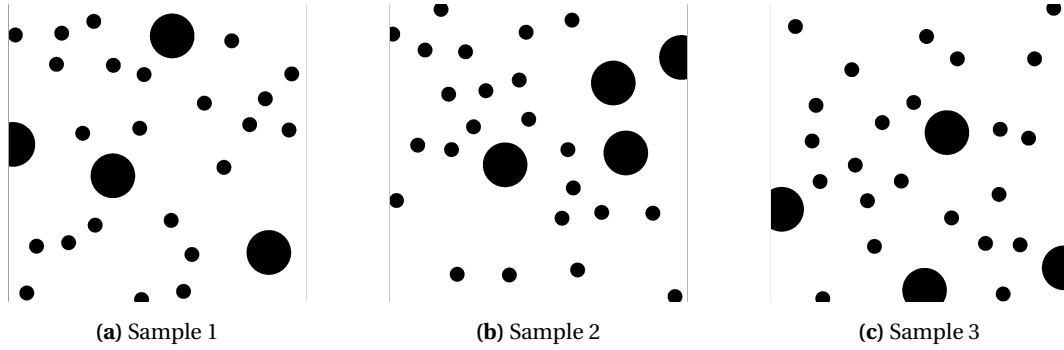


Figure 11. Three sampling used to analyse the influence and robustness of the \mathcal{V}_H protocol.

showed that they are equivalent to simulations at $\dot{\epsilon} = 10^5 \text{ s}^{-1}$.

Stress-strain curves are plotted in Figure 12 and the UTS evolution with strain rates for each sample is presented in Figure 13.

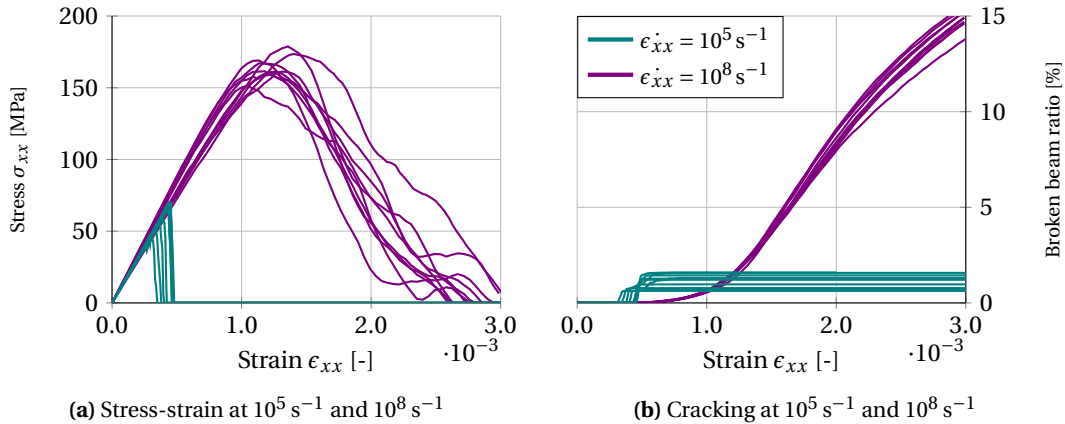


Figure 12. Evolution of stress and broken beam ratio for random samples with the \mathcal{V}_H condition.

Results are consistent with each other, confirming the robustness of the model and the boundary conditions. UTS evolution shows a scattering that does not evolve with the strain rate (standard deviation at $\dot{\epsilon} = 10^5 \text{ s}^{-1}$ is 8.3 MPa and at $\dot{\epsilon} = 10^8 \text{ s}^{-1}$ it is 7.6 MPa). As it is observed in real microstructure, for example in [3], this scattering should be reduced when the strain rate increases. This phenomenon is explained by the “weakest-link” theory: at low strain rate, the strength is determined by the most critical defect (usually the biggest porosity), which initiates the first crack at the lowest stress. As there is inherent variation in microstructures, the most critical defect may vary a lot across samples, inducing variation in UTS. At higher strain rates, the strength is affected by more defects, and it is rather the distribution of defects that controls the strength, this distribution being the same for all samples, values at high strain rates are less scattered. This is not observed in our simulations, and a possible explanation is the simplified porosity size distribution, which is discrete with only two possible values, whereas in real material the distributions are continuous with often a Gaussian form. Hence, in our simulation, the most critical defect (largest pore) is always the same. Of note, pore locations still induce different stress

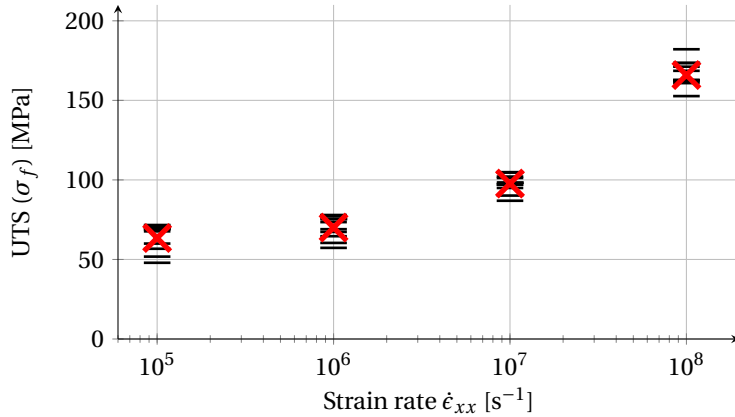


Figure 13. Ultimate tensile stress as a function of strain rate for all samples using the \mathcal{V}_H protocol. Mean value for each strain rate is indicated by a red cross.

concentrations and thus slight variations. Nevertheless, the diminution of the scattering effect with the strain rate is well described by the model by looking at the cracking evolution (broken beam ratio) in the Figure 12(b). Here, rather than observing a high variability at $10^5 s^{-1}$ (due to the above explanation), a reduced scattering on the damage evolution is well observed for higher strain rate at $10^8 s^{-1}$. Indeed, at a low strain rate, there is a certain dispersion of strain level at the start of crack propagation (when the first beam breaks), and it is linked to the maximal tensile stress, as samples that start to crack first will reach lower maximal stress. Final crack density also varies, and this is due to the difference in porosity layout, which will induce different crack paths even though the failure at low strain rate results in a main crack across the sample. At higher strain rate, the cracking starts at the same strain (respectively for each sample). However, due to the multi-fragmentation process, cracking evolution follows almost the same trend with lower dispersion than results at lower strain rate. All these observations are in very good accordance with theoretical knowledge and observations about the fragmentation process in brittle materials and the influence of the tensile strain rate.

7. Phenomenological analysis

This section is dedicated to the in-depth understanding of underlying phenomenon that lead to the observed macroscopic increase of failure stress with increasing strain rate. All following simulations are performed with the \mathcal{V}_H protocol.

7.1. Time delay effect

At incipient failure, stress is released around the cracked zone. The information that the failure appended (i.e. the release wave) take some time to reach an edge where the macroscopic stress is measured. Meanwhile, the macroscopic stress is still increasing, and all the faster as the strain rate increases. Hence, one can assume that the information speed (i.e. stress wave celerity C_L) is a key parameter regarding the increase of UTS with strain rate.

To study the influence of wave celerity, additional simulations are performed with the same model (numerical domain and parameters) as described in Section 4.2, only the macroscopic elastic modulus E and density ρ are modified independently. As a consequence, the time step is

adjusted to always respect the CFL condition. Results in terms of UTS with respect to strain rate are presented on Figure 14 and compared to the reference ($\rho^* = 5365 \text{ kgm}^{-3}$ and $E^* = 150 \text{ GPa}$). According to Figure 14(a), when the density increases, the UTS increases. Also, when the density increases, the wave celerity decreases (equation (1)), hence the information takes more time to propagate and the UTS can increase more. We might expect the opposite effect when the elastic modulus increases, as it leads to an increasing of the wave celerity. However, this is not what is observed on Figure 14(b), where the UTS increases with increasing modulus. In fact, one has also to consider the stress rate $\dot{\sigma} = E \times \dot{\epsilon}$, which increases when the elastic modulus increases. Hence, even if the information travels faster (leaving less time for stress to increase), the stress also increases faster. There is a root-square difference between these two phenomena, leading to the same influence of elastic modulus and density as demonstrated by equation (20):

$$\frac{\dot{\sigma}(E)}{C_L(E)} \propto \frac{E}{\sqrt{E}} = \sqrt{E} \quad \text{and} \quad \frac{\dot{\sigma}(\rho)}{C_L(\rho)} \propto \sqrt{\rho}. \quad (20)$$

All simulations follow precisely the same power law which confirms that the UTS evolves with the square root of the density and elastic modulus (as established by equation (20)). This result is in line with work from Kimberley [1] where a characteristic strain rate is expressed as a function of wave celerity and elastic modulus and leads to the same conclusions.

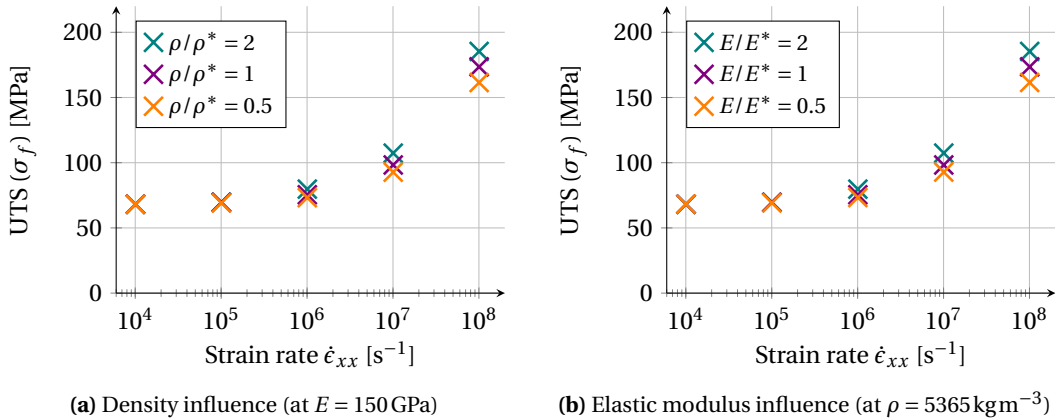


Figure 14. UTS as a function of strain rate with VH protocol for sample with different density or elastic modulus (references values denoted by *).

On Figure 15 the results are normalized by $\dot{\epsilon}_{0xx}(\rho)$ obtained from equation (21):

$$\dot{\epsilon}_{0xx}(\rho) = \dot{\epsilon}_{0xx}^* \times \sqrt{\frac{\rho^*}{\rho}} \quad \text{and} \quad \dot{\epsilon}_{0xx}(E) = \dot{\epsilon}_{0xx}^* \times \sqrt{\frac{E^*}{E}}, \quad (21)$$

where $\dot{\epsilon}_{0xx}^* = 5.3 \times 10^7 \text{ s}^{-1}$ has been determined in Section 6.1.

7.2. Sample size influence

The stress wave velocity affects the UTS as demonstrated in the previous section. In a “time delay” paradigm, the travel distance (i.e. sample size) could also affects the UTS. However, as long as the sample is a representative volume element (RVE) its size should not modify the computed behavior. To verify this crucial feature, simulations are performed on samples with the same parameters as of Section 4.1 but with increased size, up to $4 \mu\text{m}$.

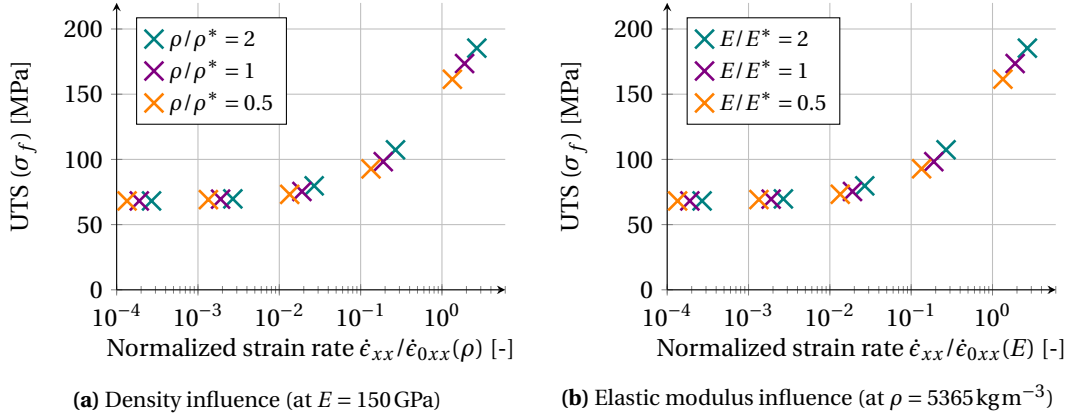


Figure 15. UTS as a function of strain rate with VH protocol for sample with different density or elastic modulus and normalized strain rates.

For the sake of simplicity, the assumption of a periodic material has been made. This allows to conduct new tests on only one sample per new size, as in periodic materials the elementary cell is by definition an RVE. Whereas in the case of non-periodic materials, we would have had to verify that our first sample is an RVE or carry out a statistical study on a sufficient number of samples. The selected elementary cell is the first sample of dimension $1\ \mu\text{m}$ by $1\ \mu\text{m}$ from Section 4.2, others samples are generated by reproducing the same microstructure (pore location and size). Moreover, the sample length is only increased in the loading direction for three reasons. First, this is the only dimension involved in strain rate computation (equation (12)) and equilibrium time (equation (5)) that could potentially affect the results. Secondly, as the microstructure is periodic, increasing the length in the direction perpendicular to the loading direction is equivalent to performing several iterations of the same test in parallel, which will obviously lead to the same results. Finally, increasing the length only in the loading direction allows to save some computation time as fewer elements are involved.

Simulation for various strain rates are performed on each new sample with the \mathcal{V}_H protocol and stress-strain relations are plotted on Figure 16.

One can observe that samples of length $2\ \mu\text{m}$ and $4\ \mu\text{m}$ have a lower UTS compared to samples of length $1\ \mu\text{m}$ and $3\ \mu\text{m}$ at $\dot{\epsilon}_{xx} = 10^5\ \text{s}^{-1}$: 57 MPa for $L_x = 2\ \mu\text{m}$ and 68 MPa for $L_x = 1\ \mu\text{m}$ (Figure 16(a)). The measured UTS are reported on Figure 17, where despite the variation in UTS (below 10 % for each strain rate), each sample follows the same evolution and no clear influence of the sample length can be observed.

This difference is attributed to the inherent randomness induced by DEM: for the same applied macroscopic stress, the stress in the bonds surrounding porosities is not exactly the same across all samples. This leads to different macroscopic failure stress because the crack propagation is controlled by a stress criterion at the bond scale. However, this effect remains limited because DE are sufficiently small facing the porosities. This difference is decreasing for increasing strain rate until $10^7\ \text{s}^{-1}$. At $10^8\ \text{s}^{-1}$, the UTS of sample $L_x = 2\ \mu\text{m}$ is higher (187 MPa) than that of sample $L_x = 1\ \mu\text{m}$ (174 MPa).

Figure 18 shows fragmented samples at the end of simulation and explains why the sample length has no effect on the UTS.

At low strain rate (Figures 18(a) and 18(c)) each periodic cell generates a macroscopic crack. Different crack paths are observed due to the randomness induced by DEM, however the cracks still initiate from the biggest porosities and follow a similar pattern. In the sample with $L_x = 2\ \mu\text{m}$

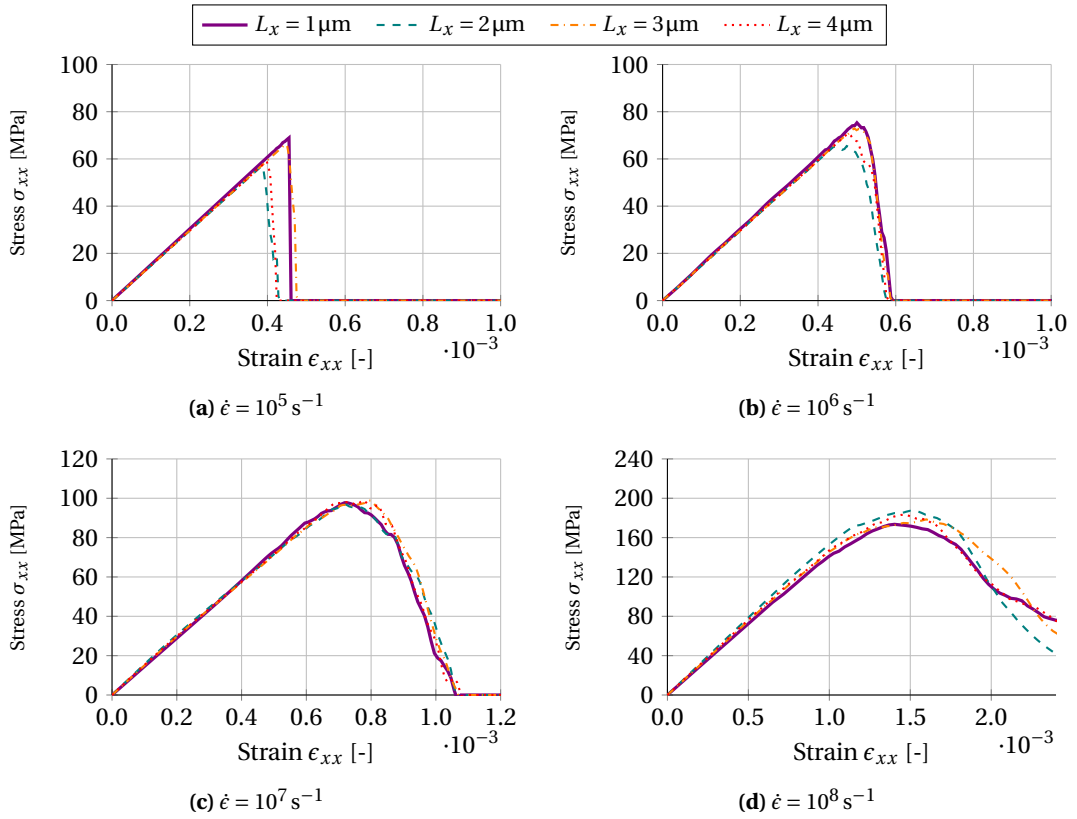


Figure 16. Stress-strain comparison for different sample length.

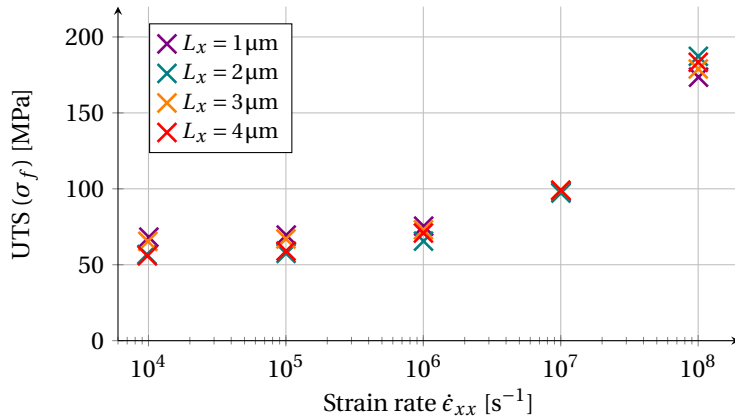


Figure 17. UTS for the different sample length.

(Figure 18(a)), even if the length is twice higher, the obscured zone does not take more time to spread as there are two main cracks that are developing in parallel. In the sample with $L_x = 3 \mu\text{m}$ (Figure 18(c)), even if the cracking pattern is more complex, three main cracks in vertical direction are also present in each cell.

At higher strain rates (Figures 18(b) and 18(d)) all porosities initiate cracks, which tends to

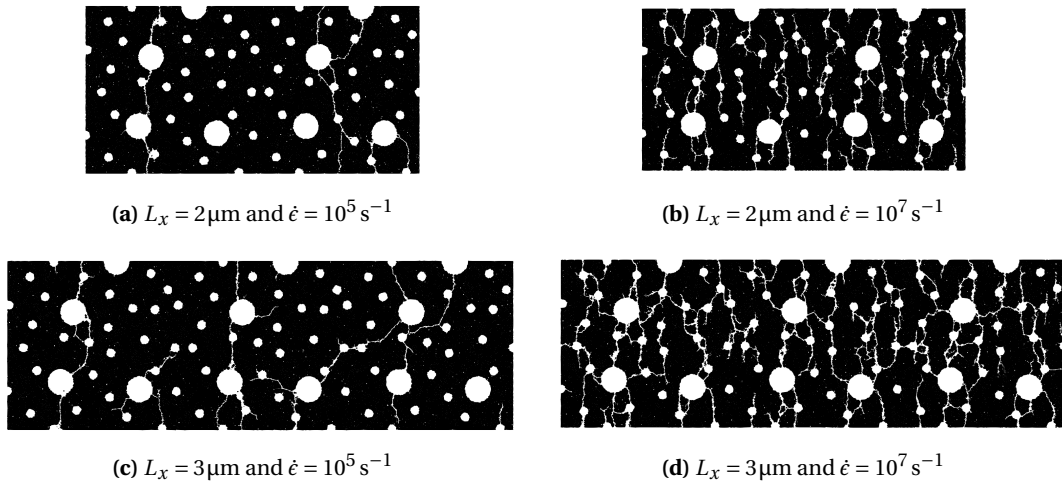


Figure 18. Fragmentation of the sample with $L_x = 2\mu\text{m}$ (a,b) and $L_x = 3\mu\text{m}$ (c,d) at $\dot{\epsilon} = 10^5\text{s}^{-1}$ and $\dot{\epsilon} = 10^7\text{s}^{-1}$.

decrease the impact of the first cracks and their paths on the UTS, leading to less dispersed results.

8. Application on a 3D sample with real microstructure

As a demonstration of the capability of the developed protocol, it has been applied to a 3D model of a real microstructure. The selected material is a plasma-sprayed yttria-stabilized-zirconia (YSZ) ceramic coating. Its 3D microstructure is obtained via FIB-SEM observation and image processing is used to extract porosities: pores and also nano-cracks already present in the initial unloaded material (Figure 19). These porosities are reproduced in a numerical sample by removing DE for the pores and modifying bond behavior for the initial cracks. The numerical sample size is $18 \times 13 \times 21 \mu\text{m}^3$, it is discretized with 92000 DE of mean radius $0.2\mu\text{m}$. More information can be found in our previous paper [20].

Uniaxial tensile tests are performed along the \vec{z} direction (see Figure 19) with the \mathcal{V}_H protocol for strain rates between $1.2 \times 10^4\text{s}^{-1}$ and $1.2 \times 10^8\text{s}^{-1}$. Stress-strain curves and broken beam ratio are presented in Figure 20, ultimate tensile stresses are plotted in Figure 21. The fracture parameters have not been finely calibrated, so the fracture stress in static regime (σ_0) at $\dot{\epsilon} = 1.2 \times 10^4\text{s}^{-1}$ is very high with a value of 775 MPa, hence all stress values are normalized by σ_0 . On Figure 21 the strain rate has been normalized by $\dot{\epsilon}_0 = 2.7 \times 10^7\text{s}^{-1}$, this value is obtained by achieving the best fit with Kimberley's power law [1], which is plotted in a dashed line. Fragmentation patterns are presented for two strain rates in Figure 22.

The maximal tensile stress increase with strain rate (Figure 20) by a factor of two between $1.2 \times 10^4\text{s}^{-1}$ and $1.2 \times 10^8\text{s}^{-1}$. Fragmentation pattern is also evolving with strain rate, a main crack perpendicular to the loading direction is visible at lower strain rate in Figure 22(a), while a lot of cracks are present at higher strain rate (Figure 22(b)).

The ultimate stress increases between tests at $1.2 \times 10^7\text{s}^{-1}$ and $1.2 \times 10^8\text{s}^{-1}$ (Figure 20(a)) but the UTS value at $1.2 \times 10^8\text{s}^{-1}$ is far below the prediction of Kimberley law. According to Figure 20(b) the cracking evolution at $1.2 \times 10^7\text{s}^{-1}$ and $1.2 \times 10^8\text{s}^{-1}$ are the same. This saturation of the cracking evolution might be responsible for the difference observed at high strain rate. However, it is difficult to explain the cause of this saturation solely from this results and whether

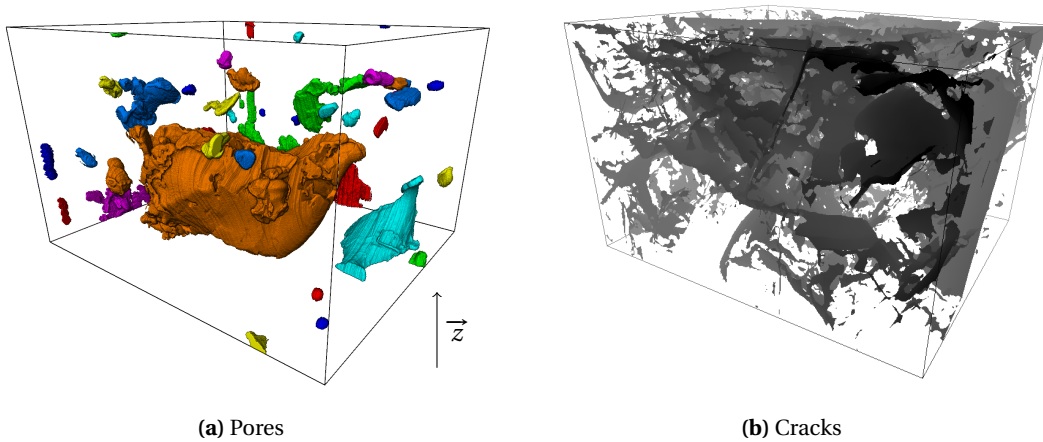


Figure 19. Microstructure of a plasma-sprayed YSZ ceramics reconstructed from FIB-SEM observation and image processing (volume dimension are $18 \times 13 \times 21 \mu\text{m}^3$).

it is due to the microstructure of this material which contains a lot of pre-existing cracks or numerical limitation of the model.

Although the 3D results cannot be used directly or compared with experimental values, notably because the volume size is too small to be representative and the static breaking stress has not been calibrated, the trends and phenomena previously observed in 2D are also obtained on the 3D sample. This validates the protocol and the robustness of the method on a 3D configuration with a complex microstructure composed of pores and numerous initial cracks.

9. Conclusion

Numerical simulations of tensile tests on brittle heterogeneous materials have been performed at the microstructure scale to study the effect of strain rate on tensile strength. A specific protocol has been developed to ensure a stress equilibrium state during the simulations. This

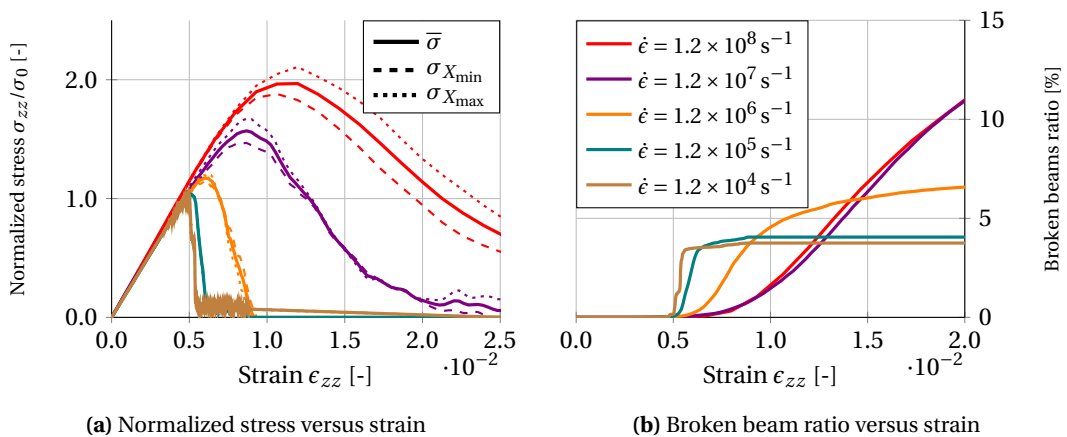


Figure 20. Evolution of stress and broken beam ratio for the 3D sample of YSZ at several strain rate.

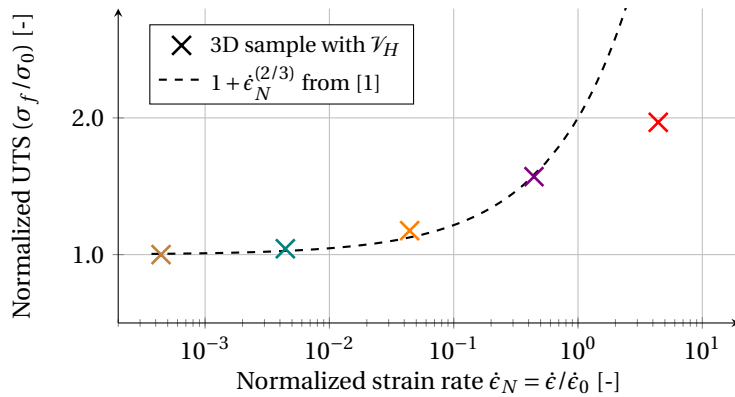


Figure 21. Ultimate tensile stress for the 3D sample of YSZ ($\sigma_0 = 775 \text{ MPa}$ and $\dot{\epsilon}_0 = 2.7 \times 10^7 \text{ s}^{-1}$).

is achieved by applying an initial velocity field, which takes into account the heterogeneity of the microstructure and ensures a constant strain rate during the simulations. Strain rate effects are successfully observed on idealised 2D models although no strain rate dependency is implemented in the behavior law or simulation code. The developed protocol shows great superiority compared to other solutions which either do not allow the target strain rate to be reached, or cause parasitic effects.

The numerical results show that maximum stress and crack density increase with strain rate as reported in literature. The observation of the stress fields and cracking during the test confirms

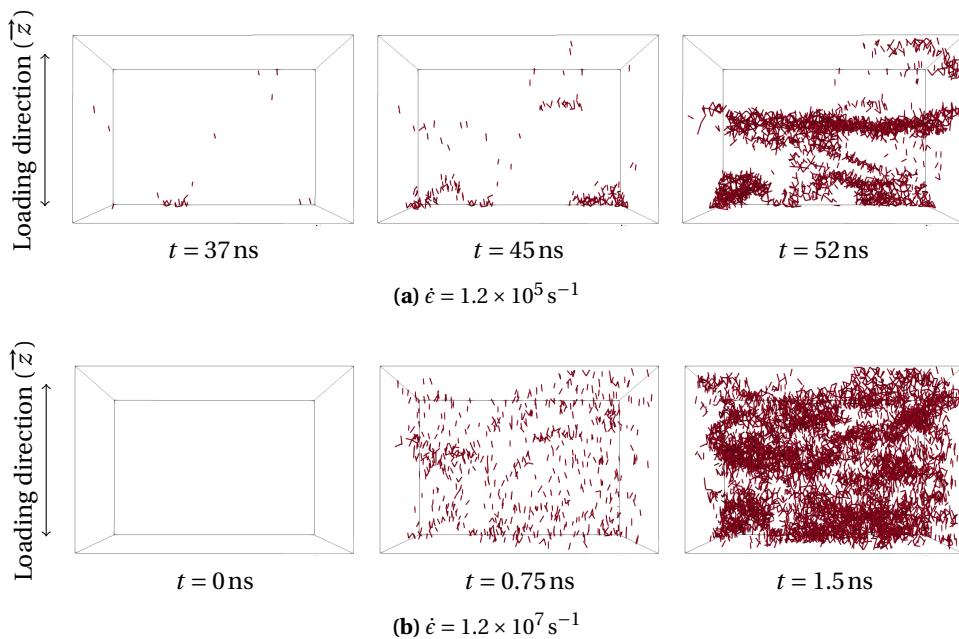


Figure 22. Cracking in 3D sample at two strain rates, only broken beams (that represent cracks) are displayed in red.

that an obscuration phenomenon is at the origin of these trends, meaning that the proposed model is able to capture such complex phenomenon. The results are sample size independent as long as RVE are considered. Both material density and elastic modulus have the same influence on tensile strength by modifying the stress wave celerity and stress rate loading.

These DEM simulations improve our understanding of the mechanisms involved in dynamic fragmentation. Besides, it is possible to consider the construction of a damage model at the macroscopic scale via a multi-scale approach.

In future works, it would be interesting to investigate the effects of porosity populations on the evolution of the maximum stress, using random distribution function already deployed to generate realistic numerical microstructures. However, the last section of this paper shows a high efficiency of the model to simulate fragmentation mechanisms directly from real 3D scans of a very complex microstructure, thus paving the way for new prospects in the development of new materials that are more resistant to impact and shock.

Acknowledgments

The manuscript was written through contributions of all authors.

Declaration of interests

The authors do not work for, advise, own shares in, or receive funds from any organization that could benefit from this article, and have declared no affiliations other than their research organizations.

References

- [1] J. Kimberley, K. T. Ramesh and N. P. Daphalapurkar, "A scaling law for the dynamic strength of brittle solids", *Acta Mater.* **61** (2013), no. 9, pp. 3509–3521.
- [2] C. Denoual and F. Hild, "A damage model for the dynamic fragmentation of brittle solids", *Comput. Methods Appl. Mech. Eng.* **183** (2000), pp. 247–258.
- [3] P. Forquin, "Brittle materials at high-loading rates: an open area of research", *Philos. Trans. R. Soc. Lond., Ser. A* **375** (2017), no. 2085, article no. 20160436 (12 pages).
- [4] G. Z. Voyiadjis (ed.), *Handbook of damage mechanics: nano to macro scale for materials and structures. Vol. 2*, Springer, 2022.
- [5] G. Ravichandran and G. Subhash, "A micromechanical model for high strain rate behavior of ceramics", *Int. J. Solids Struct.* **32** (1995), no. 17–18, pp. 2627–2646.
- [6] Z. Song and Y. Lu, "Mesoscopic analysis of concrete under excessively high strain rate compression and implications on interpretation of test data", *Int. J. Impact Eng.* **46** (2012), pp. 41–55.
- [7] P. Forquin, M. C. Blasone, D. Georges and M. Dargaud, "Continuous and discrete methods based on X-ray computed-tomography to model the fragmentation process in brittle solids over a wide range of strain-rates - application to three brittle materials", *J. Mech. Phys. Solids* **152** (2021), article no. 104412.
- [8] N. P. Daphalapurkar, K. T. Ramesh, L. Graham-Brady and J.-F. Molinari, "Predicting variability in the dynamic failure strength of brittle materials considering pre-existing flaws", *J. Mech. Phys. Solids* **59** (2011), no. 2, pp. 297–319.
- [9] B. Paliwal and K. T. Ramesh, "An interacting micro-crack damage model for failure of brittle materials under compression", *J. Mech. Phys. Solids* **56** (2008), no. 3, pp. 896–923.
- [10] X. Song, J. Zhang, C. Lin, Z. Liu, C. Jiang, M. Kong and Y. Zeng, "Microstructures and residual strain/stresses of YSZ coatings prepared by plasma spraying", *Mater. Lett.* **240** (2019), pp. 217–220.
- [11] G. Bruno and M. Kachanov, "Microstructure-property connections for porous ceramics: the possibilities offered by micromechanics", *J. Am. Ceram. Soc.* **99** (2016), no. 12, pp. 3829–3852.
- [12] F. Gatuingt, L. Snozzi and J.-F. Molinari, "Determination of the dynamic tensile response and dissipated fracture energy of concrete with a cohesive element model", 2012. Online at <https://hal.science/hal-01624529>. Conference paper from *International Conference on numerical modeling strategies for sustainable concrete structures – SSCS 2012*.

- [13] Y. J. Huang, Z. J. Yang, X. W. Chen and G. H. Liu, "Monte Carlo simulations of meso-scale dynamic compressive behavior of concrete based on X-ray computed tomography images", *Int. J. Impact Eng.* **97** (2016), pp. 102–115.
- [14] C. Qin and C. Zang, "Numerical study of dynamic behavior of concrete by meso-scale particle element modeling", *Int. J. Impact Eng.* **38** (2011), pp. 1011–1021.
- [15] D. Liu, B. Šavija, G. E. Smith, P. E. J. Flewitt, T. Lowe and E. Schlangen, "Towards understanding the influence of porosity on mechanical and fracture behaviour of quasi-brittle materials: experiments and modelling", *Int. J. Fract.* **205** (2017), pp. 57–72.
- [16] P. Forquin and F. Hild, "A probabilistic damage model of the dynamic fragmentation process in brittle materials", in *Advances in applied mechanics* (H. Aref and E. van der Giessen, eds.), Advances in Applied Mechanics, vol. 44, Elsevier, 2010, pp. 1–72.
- [17] M. Sage, J. Girardot, J.-B. Kopp and S. Morel, "A damaging beam-lattice model for quasi-brittle fracture", *Int. J. Solids Struct.* **239–240** (2022), article no. 111404 (18 pages).
- [18] F. Asadi, D. André, S. Emam, P. Doumalin and M. Huger, "Numerical modelling of the quasi-brittle behaviour of refractory ceramics by considering microcracks effect", *J. Eur. Ceram. Soc.* **42** (2022), no. 3, pp. 1149–1161.
- [19] N. Ferguen, Y. Mehdoua-Lahmar, H. Lahmar, W. Leclerc and M. Guessasma, "DEM model for simulation of crack propagation in plasma-sprayed alumina coatings", *Surf. Coat. Technol.* **371** (2019), pp. 287–297.
- [20] V. Longchamp, J. Girardot, D. André, F. Malaise, A. Quet, P. Carles and I. Iordanoff, "Discrete 3D modeling of porous-cracked ceramic at the microstructure scale", *J. Eur. Ceram. Soc.* **44** (2024), no. 4, pp. 2522–2536.
- [21] Y. Yu, X. Cao, J. Yang, Y. Li, W. Wang and H. He, "Delayed fracture of porous ceramics under shock-wave compression", *Eng. Fract. Mech.* **208** (2019), pp. 38–44.
- [22] L. Brémaud, J. Girardot, P. Forquin and F. Malaise, "Simulation of shockless spalling fragmentation using the Discrete Element Method (DEM)", *Eur. J. Mech. A Solids* **115** (2026), article no. 105804 (12 pages).
- [23] X. Zhou, Y. Xie, G. Long, X. Zeng, J. Li, L. Yao, W. Jiang and Z. Pan, "DEM analysis of the effect of interface transition zone on dynamic splitting tensile behavior of high-strength concrete based on multi-phase model", *Cem. Concr. Res.* **149** (2021), article no. 106577.
- [24] X. Li, Y. Liang and Y. Qian, "3D DEM framework for simulating the influence of aggregate strength on the dynamic splitting tensile fracture behavior of concrete", *Comput. Part. Mech.* (2025).
- [25] C. A. Ross, J. W. Tedesco and S. T. Kuennen, "Effects of strain rate on concrete strength", *ACI Mater. J.* **92** (1995), no. 1, pp. 37–47.
- [26] D. L. Grote, S. W. Park and M. Zhou, "Dynamic behavior of concrete at high strain rates and pressures: I. experimental characterization", *Int. J. Impact Eng.* **25** (2001), no. 9, pp. 869–886.
- [27] X. Zhang, B. Fatahi, H. Khabbaz and H. Zhang, "Investigating effects of fracture density on stress-strain behaviour of jointed rocks using Discrete Element Method", 2017. Online at https://www.researchgate.net/publication/320887955_Investigating_Effects_of_Fracture_Density_on_Stress-Strain_Behaviour_of_Jointed_Rocks_Using_Discrete_Element_Method.
- [28] K. Radi, D. Jauffrès, S. Deville and C. L. Martin, "Elasticity and fracture of brick and mortar materials using discrete element simulations", *J. Mech. Phys. Solids* **126** (2019), pp. 101–116.
- [29] D. André, J.-I. Charles, I. Iordanoff and J. Néauport, "The GranOO workbench, a new tool for developing discrete element simulations, and its application to tribological problems", *Adv. Eng. Softw.* **74** (2014), pp. 40–48.
- [30] D. André, I. Iordanoff, J.-I. Charles and J. Néauport, "Discrete element method to simulate continuous material by using the cohesive beam model", *Comput. Methods Appl. Mech. Eng.* **213–216** (2012), pp. 113–125.
- [31] D. André, M. Jebahi, I. Iordanoff, J.-I. Charles and J. Néauport, "Using the discrete element method to simulate brittle fracture in the indentation of a silica glass with a blunt indenter", *Comput. Methods Appl. Mech. Eng.* **265** (2013), pp. 136–147.
- [32] F. Asadi, D. André, S. Emam, P. Doumalin and M. Huger, "Numerical modelling of the quasi-brittle behaviour of refractory ceramics by considering microcracks effect", *J. Eur. Ceram. Soc.* **42** (2022), no. 3, pp. 1149–1161.
- [33] F. Zhou and J.-F. Molinari, "Stochastic fracture of ceramics under dynamic tensile loading", *Int. J. Solids Struct.* **41** (2004), no. 22–23, pp. 6573–6596.
- [34] J.-L. Le, J. Eliáš, A. Gorgogianni, J. Vievering and J. Květoň, "Rate-dependent scaling of dynamic tensile strength of quasibrittle structures", *J. Appl. Mech.* **85** (2017), no. 2, article no. 021003 (12 pages).